Zn(Ta$_{1-x}$Nb$_x$)$_2$O$_6$ nanomaterials. Synthesis, characterization and corrosion behaviour

MIHAELA BIRDEANU[1,2*], GHEORGHE FAGADAR-COSMA[2], IULIANA SEBARCHIEVICI[1], AUREL - VALENTIN BIRDEANU[3], BOGDAN TARANU[1], IOAN TARANU[1] and EUGENIA FAGADAR-COSMA[4]

[1]*National Institute for Research and Development in Electrochemistry and Condensed Matter, 1 Plautius Andronescu Street, 300224 Timisoara, Romania, [2]Politehnica University of Timisoara, Vasile Parvan Ave.6, 300223-Timisoara, Romania, [3]National R&D Institute for Welding and Material Testing - ISIM Timişoara, 20 M. Viteazu Ave., 300222, Timisoara, Romania and [4]Institute of Chemistry Timisoara of Romanian Academy, 24 M. Viteazu Ave, 300223-Timisoara, Romania*

*Corresponding author. Tel: +40 256-494413, Fax: +40 256-204698
E-mail address: mihaelabirdeanu@gmail.com

Abstract: Zn(Ta$_{1-x}$Nb$_x$)$_2$O$_6$ pseudo-binary oxide nanocrystalline materials (where x = 1; 0.5; 0.1; 0.05 and 0) were obtained through the solid-state method and characterized by X-ray diffraction, Fourier Transform Infrared Spectroscopy and Ultraviolet-visible spectroscopy. In addition, their morphology and topography have been determined by field emission-scanning electron microscopy (SEM) and atomic force microscopy (AFM). There is a significant dependence between the rugosity and the uniformity of crystals. The evenly crystals organized in multilayers have the lowest value of rugosity and the non uniform fractal type architectures have the highest value of rugosity. The compounds' anti-corrosion features were evaluated after deposition on carbon steel (OL) in 0.1 M Na$_2$SO$_4$ media by open circuit potential measurement and potentiodynamic polarization technique with Tafel representation. The inhibition efficiency of pseudo-binary oxides deposited on carbon steel electrode was in the range 42.3-52.7 % promising for their further multiple layer deposition with porphyrins in order to improve anticorrosion properties. Due to the high band gap (3.80 - 4.30 eV) provided by increasing the

tantalum content, four of these pseudo-binary oxides might find applications in photovoltaic cells.

Keywords: nanomaterials, solid-state method, pseudo-binary oxides, corrosion inhibition, Tafel curves

RUNNING TITLE: PSEUDO-BINARY OXIDES NANOMATERIALS

INTRODUCTION

A widely used material in many industries, the steel[1] is prone to corrosion as a result of reactions with the environment. This spontaneous process can compromise the material integrity and might bring serious impact to the environment and that is why measures to prevent and control it are required.

Zinc is the most widely used material for protection of steel against corrosion[2-4]. Its corrosion resistance, however, is limited. Zinc alloys can create improved corrosion resistance compared to pure zinc in the protection of ferrous-based metals[5-9]. The efforts to improve the corrosion stability of pure zinc coatings have been directed toward alloying with more noble metal or adding surface inhibitors[10]. Recently, niobium and tantalate oxides were applied in chemical processing applications due to their outstanding corrosion resistance[11-13].

The binary niobate and tantalate compounds with general formula $Zn(Ta_{1-x}Nb_x)_2O_6$ were found to be promising candidates for application in microwave devices based on the improved dielectric properties of these compounds revealing both high quality factor ($Q \times f$) and dielectric constant (ε_r)[14-18].

$ZnTa_2O_6$ have been obtained based on several modern chemistry preparation routes, e.g. citrate sol–gel[19], but the most used method is the conventional solid-state reaction of mixed oxides[17-21]. $Zn(Nb_{1-x}Ta_x)_2O_6$ (where x = 0; 0.2; 0.4; 0.6; 0.8; 0.9; 1) novel derivatives exhibiting remarkable dielectric properties were usually prepared by the conventional mixed oxide route[22].

The $ZnNb_2O_6$ material is also used as a dielectric[23, 24] and was obtained using the molten salt synthesis[25, 26], sol–gel method[27], solid-state reaction[23, 24, 28] and optical floating zone

61 method[29]. These materials are used in photocatalysis[30-35], for electrochemical gas sensors[36], in

62 energy storage field[37] and in solar cell formulations[38].

63 The present study was focused on obtaining of three novel pseudo-binary compounds,

64 namely: $Zn(Ta_{1-x}Nb_x)_2O_6$, (where x = 0.5; 0.1; and 0.05) and on their investigation regarding

65 structural, morphological and optical properties in comparison with the already known $ZnNb_2O_6$

66 and $ZnTa_2O_6$. The effects produced by the increased content of tantalum on the properties of

67 these novel pseudo-binary oxides are discussed. Based on our successful experience in corrosion

68 protection (inhibition efficiency up to 96 %) by bilayer depositions of $Zn_3Ta_2O_8$ or $Zn_3Nb_2O_8$

69 and 5 - (4 - pyridyl) - 10, 15, 20 - tris (phenoxy - phenyl) porphyrin or 5 - (4 - pyridyl) - 10, 15,

70 20 - tris(3, 4 - dimethoxy - phenyl) porphyrin[39] on carbon steel electrodes, another important

71 purpose was to evaluate the anticorrosion activity exhibited by thin films of these compounds on

72 carbon steel in acid environment.

73

74 EXPERIMENTAL

75

76 *Apparatus:* The structural information of the nanomaterials was obtained by X-ray diffraction on

77 a XRD, X'pert Pro MPD X-ray diffractometer using Cu Kα radiation, at room temperature. FT-

78 IR measurements have been performed on JASCO 430 FT-IR spectrometer (KBr pellets). The

79 morphology and the particle dimension of the samples were investigated by SEM / EDAX

80 (Model INSPECT S) and AFM (Model Nanosurf® EasyScan 2 Advanced Research). The band

81 gap of the nanomaterials was estimated from the diffuse reflectance spectrum, at room

82 temperature, recorded on an UV-VIS-NIR spectrometer Lambda 950. Electrochemical

83 measurements were made using a Voltalab potentiostat, Model PGZ 402. The degree of

84 inhibition efficiency *IE* (%) has been calculated on the basis of the equation[40]. For method for

85 corrosion testing and cell description see Supplementary Materials.

86 *Reagents*: The starting materials used during the synthesis of $Zn(Ta_{1-x}Nb_x)_2O_6$ (where x =

87 1; 0.5; 0.1; 0.05 and 0) pseudo-binary oxides were: tantalum (V) oxide - Ta_2O_5(99.99 %, Sigma),

88 niobium (V) oxide - Nb_2O_5 (99.99 %, Merck) and zinc oxide – ZnO (99.99 %, Merck).

89 *General method for obtaining $Zn(Ta_{1-x}Nb_x)_2O_6$ (where x = 1; 0.5; 0.1; 0.05 and 0)*

90 *nanomaterials:* $Zn(Ta_{1-x}Nb_x)_2O_6$ (where x = 1; 0.5; 0.1; 0.05 and 0) nanomaterials were obtained

91 by solid-state method varying the molar ratios (Table 1). The mixtures were afterwards heated at

92   1200 ºC for 3 h soaking time. A rate of 5ºC/min of the heating and cooling was set up for the
93   heated furnace.

94

95   Table 1. The $Zn(Ta_{1-x}Nb_x)_2O_6$ nanomaterials obtained by solid-state method

The Obtaine naomaterials	x	Molar Ratios
$ZnTa_2O_6$	0	$ZnO / Ta_2O_5 = 1 / 1$
$ZnNb_2O_6$	1	$ZnO / Nb_2O_5 = 1 / 1$
$Zn(Ta_{0.95}Nb_{0.05})_2O_6$	0.05	$ZnO / Ta_2O_5 / Nb_2O_5 = 1 / 0.95 / 0.05$
$Zn(Ta_{0.9}Nb_{0.1})_2O_6$	0.1	$ZnO / Ta_2O_5 / Nb_2O_5 = 1 / 0.9 / 0.1$
$Zn(Ta_{0.5}Nb_{0.5})_2O_6$	0.5	$ZnO / Ta_2O_5 / Nb_2O_5 = 1 / 0.5 / 0.5$

96

97   RESULTS AND DISCUSSION

98

99   *Structural characterization*

100   Figure 1 presents the X-ray diffraction patterns for: a) $ZnTa_2O_6$, b) $Zn(Ta_{0.95}Nb_{0.05})_2O_6$,
101   c) $Zn(Ta_{0.9}Nb_{0.1})_2O_6$, d) $Zn(Ta_{0.5}Nb_{0.5})_2O_6$ and e) $ZnNb_2O_6$ and it can be observed that besides
102   the main peaks associated with the $ZnTa_2O_6$ and $ZnNb_2O_6$ pure nanomaterials, some associated
103   peaks did appear (indexed with JCPDS, card No. 01-076-1827 and 01-076-1826), belonging to
104   the *Pbcn* space group.
105   The intensity of the peaks, relative to the background signal, demonstrates high purity
106   and good quality of the samples. The highest intensity peak is located at $2\theta = 30.4769$ ° for
107    $ZnTa_2O_6$ and $2\theta = 30.3424$ ° for $ZnNb_2O_6$ and they belong to the 131 for $ZnTa_2O_6$ and 311 for
108    $ZnNb_2O_6$ plane[41]. The novel structures have the highest intensity peaks located at $2\theta = 30.4569$ °
109   for $Zn(Ta_{0.95}Nb_{0.05})_2O_6$, $2\theta = 30.4273$ ° for $Zn(Ta_{0.9}Nb_{0.1})_2O_6$ and $2\theta = 30.3964$ ° for
110    $Zn(Ta_{0.5}Nb_{0.5})_2O_6$, the values belonging to the interval limited by $ZnTa_2O_6$ and $ZnNb_2O_6$.
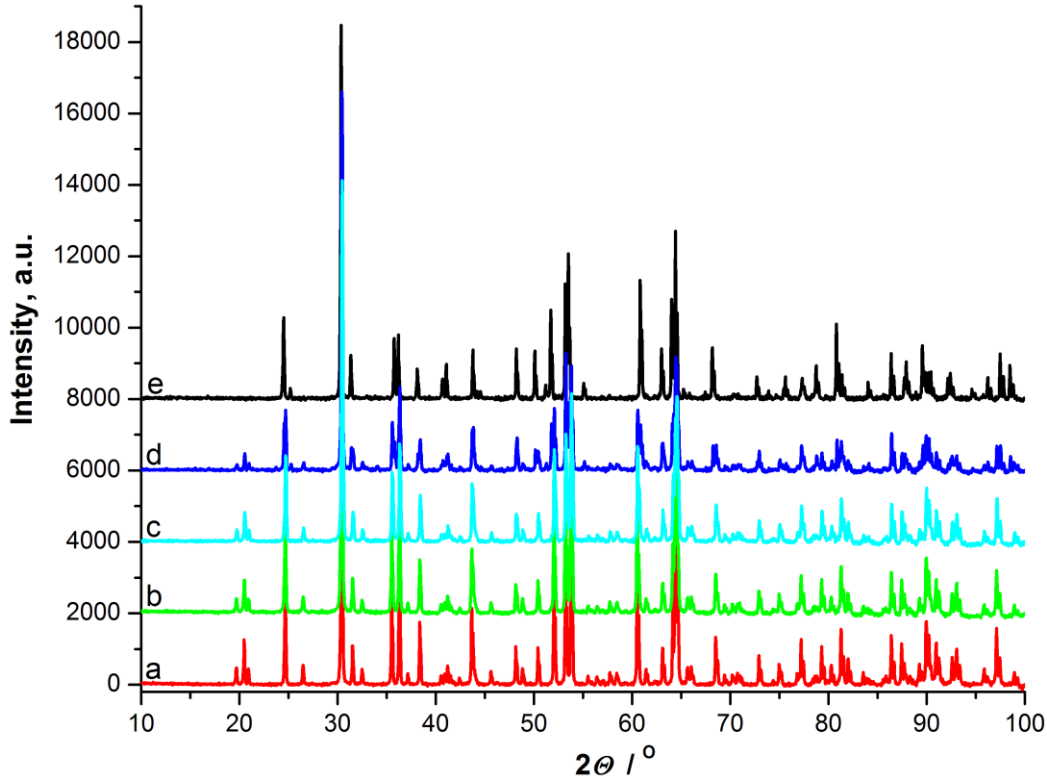
Fig. 1. The XRD patterns of (a) $ZnTa_2O_6$, (b) $Zn(Ta_{0.95}Nb_{0.05})_2O_6$, (c) $Zn(Ta_{0.9}Nb_{0.1})_2O_6$, (d) $Zn(Ta_{0.5}Nb_{0.5})_2O_6$ and (e) $ZnNb_2O_6$

The lattice constant was calculated from XRD analysis data, using FullProf Suite computer package[42]: a = 4.80 Å, b = 18.09 Å, c = 5.13 Å, α = β = γ = 90 °; elementary cell's volume (V / 10^6 / pm^3) is 409.71 for $ZnTa_2O_6$ and a = 15.30 Å, b = 5.96 Å, c = 5.14 Å, α = β = γ = 90 °; elementary cell's volume (V / 10^6 / pm^3) is 413.07 for $ZnNb_2O_6$.

The mean crystallite size (d) of the powder samples was calculated using Scherrer's equation[43]. The average crystallite size determined from XRD line broadening for each of the samples, was: 58 nm for $ZnTa_2O_6$, 47 nm for $Zn(Ta_{0.95}Nb_{0.05})_2O_6$, 42 nm for $Zn(Ta_{0.9}Nb_{0.1})_2O_6$, 39 nm for $Zn(Ta_{0.5}Nb_{0.5})_2O_6$ and 34 nm for $ZnNb_2O_6$, respectively. The values are increasing with the increase of the Ta content in the nanomaterial.

The FT-IR spectra of the obtained pseudo-binary oxides and the precursor oxides: a) $ZnNb_2O_6$, b) $ZnTa_2O_6$, c) Nb_2O_5, d) Ta_2O_5, e) ZnO, f) $Zn(Ta_{0.95}Nb_{0.05})_2O_6$, g) $Zn(Ta_{0.9}Nb_{0.1})_2O_6$ and h) $Zn(Ta_{0.5}Nb_{0.5})_2O_6$ are comparatively presented in Figure 2. The spectrum of ZnO presents a single broad and intense IR band located at wavenumber υ = 430 cm^{-1}; the spectrum of Ta_2O_5

5

128 oxide shows four broad weak absorption bands located around 900 cm^{-1}, 840 cm^{-1}, 755 cm^{-1} and

129 530 cm^{-1}; the Nb_2O_5 oxide reveals two intense not clearly separated bands at 685 cm^{-1} and 800
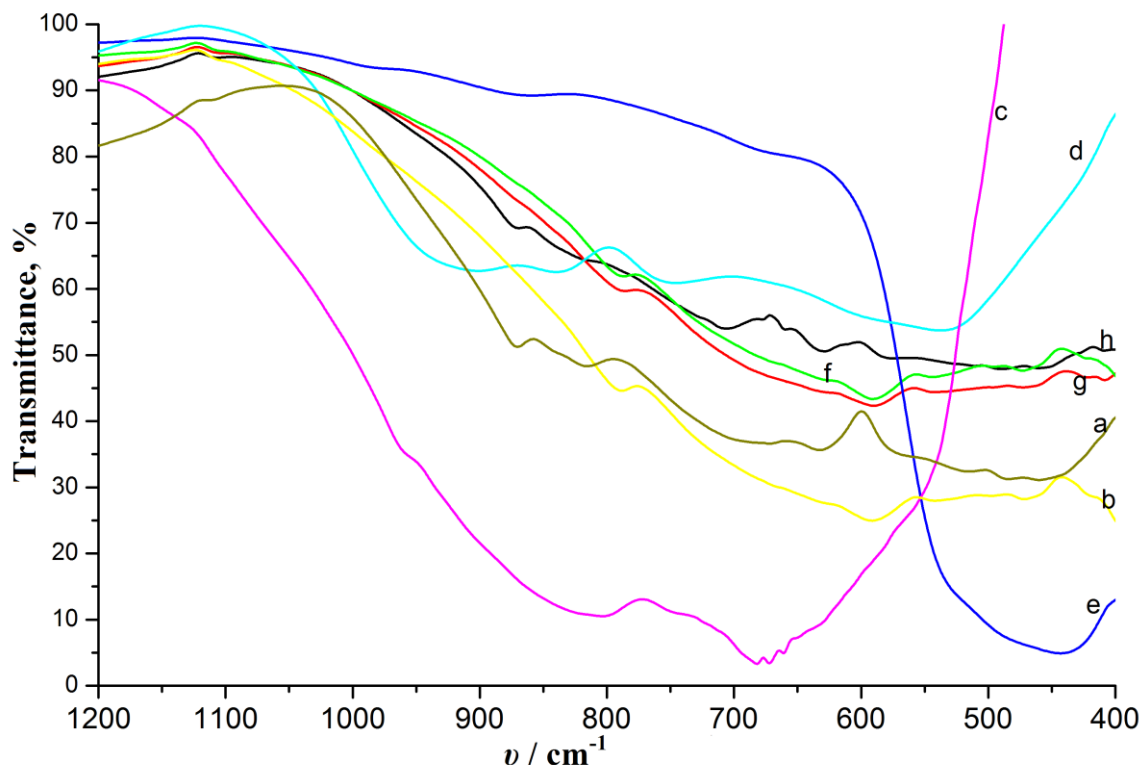
130 cm^{-1}.

131

132 Fig. 2. FT-IR spectra of the obtained (a) $ZnNb_2O_6$, (b) $ZnTa_2O_6$, (c) Nb_2O_5, (d) Ta_2O_5,

133 (e) ZnO, (f) $Zn(Ta_{0.95}Nb_{0.05})_2O_6$, (g) $Zn(Ta_{0.9}Nb_{0.1})_2O_6$ and (h) $Zn(Ta_{0.5}Nb_{0.5})_2O_6$

134

135 The FT-IR spectra of the newly obtained nanomaterials ($Zn(Ta_{1-x}Nb_x)_2O_6$ (x = 0.5; 0.1;

136 0.05) displayed some distinctive bands, located at 600 cm^{-1} [$Zn(Ta_{0.5}Nb_{0.5})_2O_6$], 620 cm^{-1}

137 [$Zn(Ta_{0.9}Nb_{0.1})_2O_6$, $Zn(Ta_{0.95}Nb_{0.05})_2O_6$], and 640 cm^{-1} [$Zn(Ta_{0.5}Nb_{0.5})_2O_6$], respectively.

138 Analyzing the structure of the novel nanomaterials and the presence of the known bands from the

139 precursor oxides, these new displayed bands at 640 cm^{-1} and at 620 cm^{-1} can be assigned to Zn-

140 O-Nb and to Zn-O-Ta novel generated bonds. As expected, these new bands are strongly

141 associated with the increased presence of each element in the structure of the nanomaterials.

142 Thus, the intensity of the peaks at 600 cm^{-1} increase with increasing of Ta content, and the

143 position of the peaks tend to be shifted towards lower wave numbers with increasing of ZnO

144 content, in agreement with reported data[21, 44]. Besides, equal molar ratios of Ta and Nb will

145 generally favor large non ressolved bands. Another aspect is that the very weak bands with peaks

146 around 540-560 cm^{-1} can be atributted to symmetrical stretching vibration modes ν_s (O–Metal–

147 O), where the metal is Ta or Nb.

148

149 *Morphological characterization*

150   The morphological aspect of the resulting powders was examined by SEM, as shown in

151 Figure 3. The micrographs for $ZnNb_2O_6$, $Zn(Ta_{0.5}Nb_{0.5})_2O_6$, $Zn(Ta_{0.9}Nb_{0.1})_2O_6$,

152 $Zn(Ta_{0.95}Nb_{0.05})_2O_6$ and $ZnTa_2O_6$ nanomaterials reveal the formation of soft spherical

153 agglomerates (a-$ZnNb_2O_6$) which display an irregular morphology or fractal-like (e-$ZnTa_2O_6$)
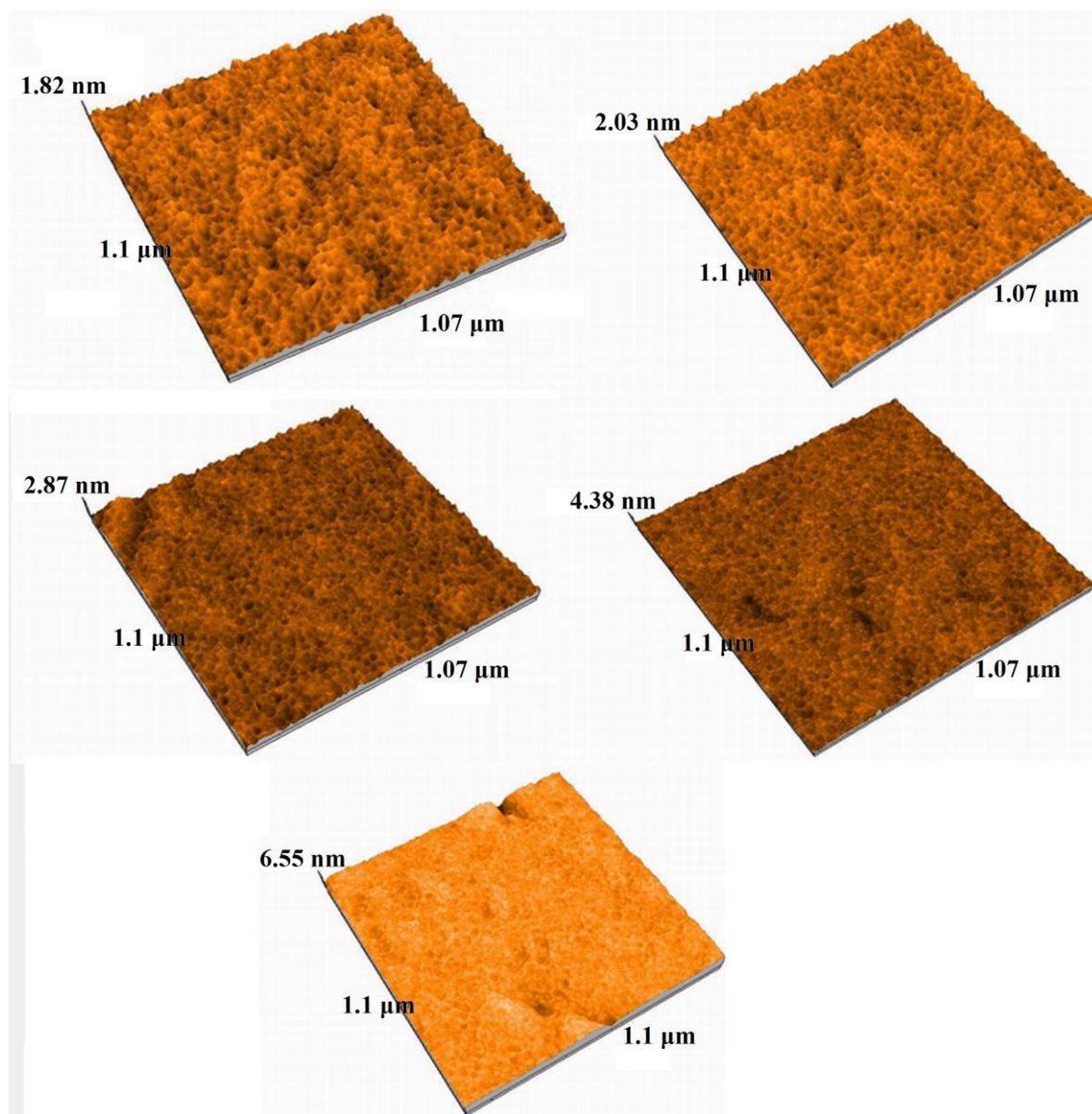
154 crystal structures.
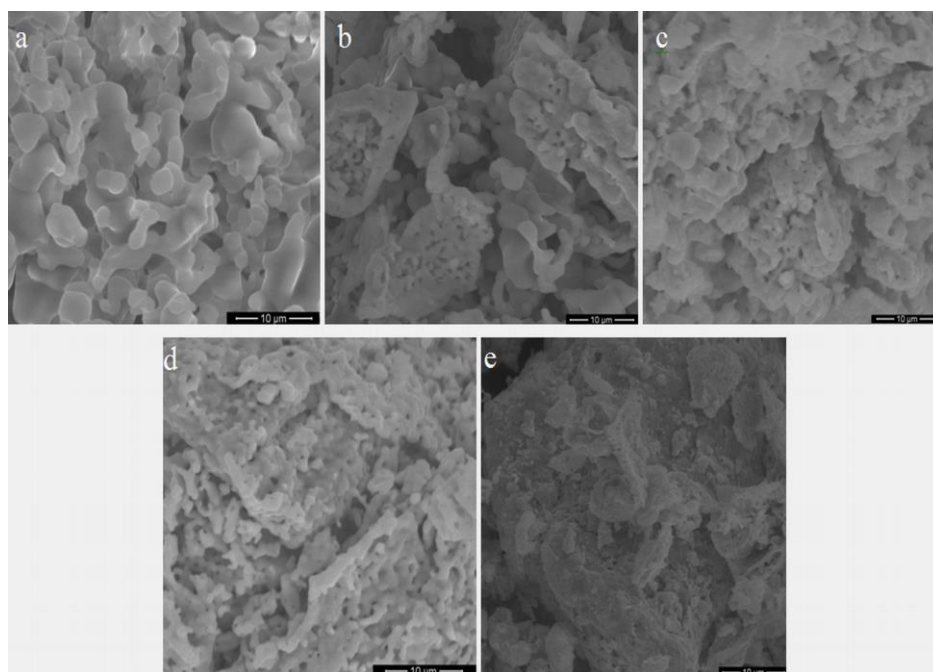
155

156   Fig. 3. The SEM images of: (a) $ZnNb_2O_6$, (b) $Zn(Ta_{0.5}Nb_{0.5})_2O_6$, (c) $Zn(Ta_{0.9}Nb_{0.1})_2O_6$, (d)

157                    $Zn(Ta_{0.95}Nb_{0.05})_2O_6$ and (e) $ZnTa_2O_6$

158

159   Depending on the nature and chemical composition of the nanomaterials the

160 morphology is different: crystals organized in multilayer as in case of $ZnNb_2O_6$, with uniform

161 covering aspect or various size distributed crystals with porous aspect (both mesopores and

162 macropores are present) or even sponge like shape in case of [b-$Zn(Ta_{0.5}Nb_{0.5})_2O_6$, c-

163 $Zn(Ta_{0.9}Nb_{0.1})_2O_6$, d-$Zn(Ta_{0.95}Nb_{0.05})_2O_6$] and going to fractal kind aspect in case of e- $ZnTa_2O_6$

164 (and a touch of amorphous aspect). The EDAX analysis certified initial molar ratios between Zn,

165 Nb and Ta see Supplementary Materials for detailed information.

166 In Figure 4 are shown the AFM images of the surface for each of the studied materials

167 deposited on OL electrodes, using a scan size of 1μm x 1μm. The contact mode cantilever was

168 used to measure the samples.

169

170 Fig. 4. AFM images of: a) $ZnNb_2O_6$, b) $Zn(Ta_{0.5}Nb_{0.5})_2O_6$, c) $Zn(Ta_{0.9}Nb_{0.1})_2O_6$, d)

171 $Zn(Ta_{0.95}Nb_{0.05})_2O_6$ and e)$ZnTa_2O_6$

172

173 The particle size analysis for $ZnNb_2O_6$, $Zn(Ta_{0.5}Nb_{0.5})_2O_6$, $Zn(Ta_{0.9}Nb_{0.1})_2O_6$,

174 $Zn(Ta_{0.95}Nb_{0.05})_2O_6$ and $ZnTa_2O_6$ deposited on OL electrodes was performed from the AFM

8

175 measurements data (Nanosurf EasyScan 2 AFM software). The average grain sizes was
176 determined, as follows: about 30 nm for $ZnNb_2O_6$, around 38 nm for $Zn(Ta_{0.5}Nb_{0.5})_2O_6$, about 45
177 nm for $Zn(Ta_{0.9}Nb_{0.1})_2O_6$, about 50 nm for $Zn(Ta_{0.95}Nb_{0.05})_2O_6$ and about 70 nm for $ZnTa_2O_6$ in
178 very good agreement with RDX measurements results. The particle size is increasing in
179 accordance with the increase of tantalum content. The surface roughness was calculated using
180 equations from[45].

181   The measured surface has an area of 1.243 pm^2. Using the Nanosurf EasyScan 2
182 computer software the values of S_a and S_q for the nanomaterials were calculated as follows: $S_a =$
183 0.21 nm and S_q = 0.38 nm for $ZnNb_2O_6$, S_a = 0.26 nm and S_q = 0.43 nm for $Zn(Ta_{0.5}Nb_{0.5})_2O_6$, S_a
184 = 0.42 nm and S_q = 0.53 nm for $Zn(Ta_{0.9}Nb_{0.1})_2O_6$, S_a = 0.53 nm and S_q = 0.89 nm for
185 $Zn(Ta_{0.95}Nb_{0.05})_2O_6$ and S_a = 0.73 nm and S_q = 1 nm for $ZnTa_2O_6$.

186   There is a strong correlation between the aspect of the samples (SEM images) and the
187 rugosity. The more uniform crystals, displayed in multilayers reflect in the lowest value of
188 rugosity and the non uniform fractal type architectures present the highest value of rugosity.
189 Some failure of the surfaces producing deep pores and channels can be noticed (Figures 5c, 5d,
190 5e).

191

192 *Optical properties*

193   Using Kubelka-Munk equation[46, 47] the absorbance was calculated from the reflectance
194 spectra (Figure 5). The diffuse reflectance spectra was also recorded (see Supplementary
195 Materials). In Figure 5 were plotted the $\{(k/s)\ hv\}^2$ versus hv, where k denotes absorption
196 coefficient, s is the scattering coefficient and hv is the photon energy. The band gap was
197 calculated and its value was: 3.20 eV for $ZnNb_2O_6$, 3.80 eV for $Zn(Ta_{0.5}Nb_{0.5})_2O_6$, 4.00 eV for
198 $Zn(Ta_{0.9}Nb_{0.1})_2O_6$, 4.10 eV for $Zn(Ta_{0.95}Nb_{0.05})_2O_6$ and 4.30 eV for $ZnTa_2O_6$. The values of band
199 gap are increasing in the same way as the increasing of inhibition of corrosion, proving the
200 differentiated chemical stability of the tested nanomaterials.

201
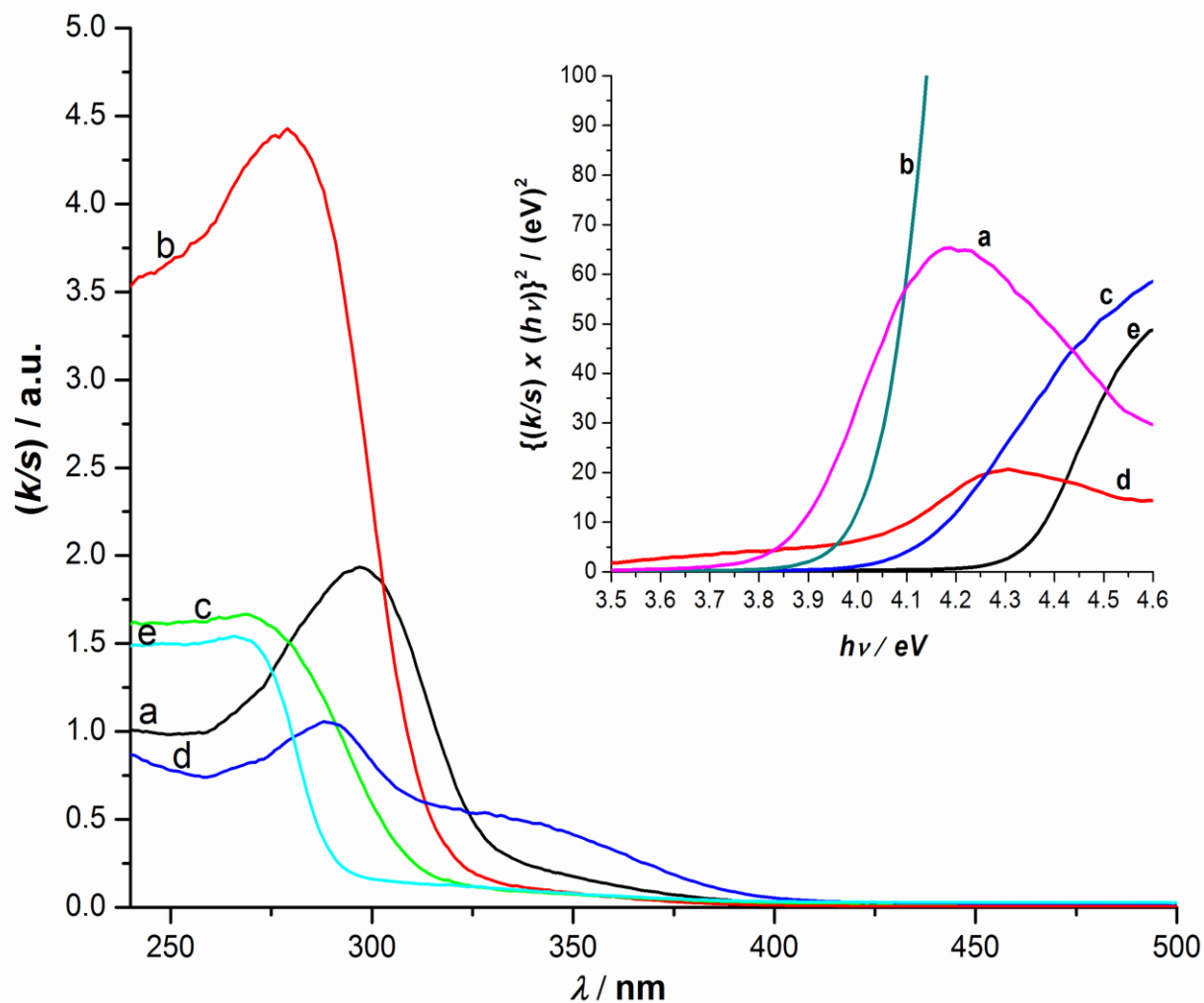
Fig. 5. Absorption spectra of: (a) $Zn(Ta_{0.5}Nb_{0.5})_2O_6$, (b) $Zn(Ta_{0.9}Nb_{0.1})_2O_6$, (c) $Zn(Ta_{0.95}Nb_{0.05})_2O_6$, (d) $ZnNb_2O_6$ and (e) $ZnTa_2O_6$. Plot of $\{(k/s)h\nu\}^2$ vs. $h\nu$ (energy) of: (a) $Zn(Ta_{0.5}Nb_{0.5})_2O_6$, (b) $Zn(Ta_{0.9}Nb_{0.1})_2O_6$, (c) $Zn(Ta_{0.95}Nb_{0.05})_2O_6$, (d) $ZnNb_2O_6$ and (e) $ZnTa_2O_6$

Tafel polarization plots

Tafel plots of the investigated OL electrodes, recorded after 30 minutes OCP (see Supplementary Materials) in 0.1 M Na_2SO_4 solution, are shown in Figure 6. The parameters calculated from these plots are summarized in Table 2.

10
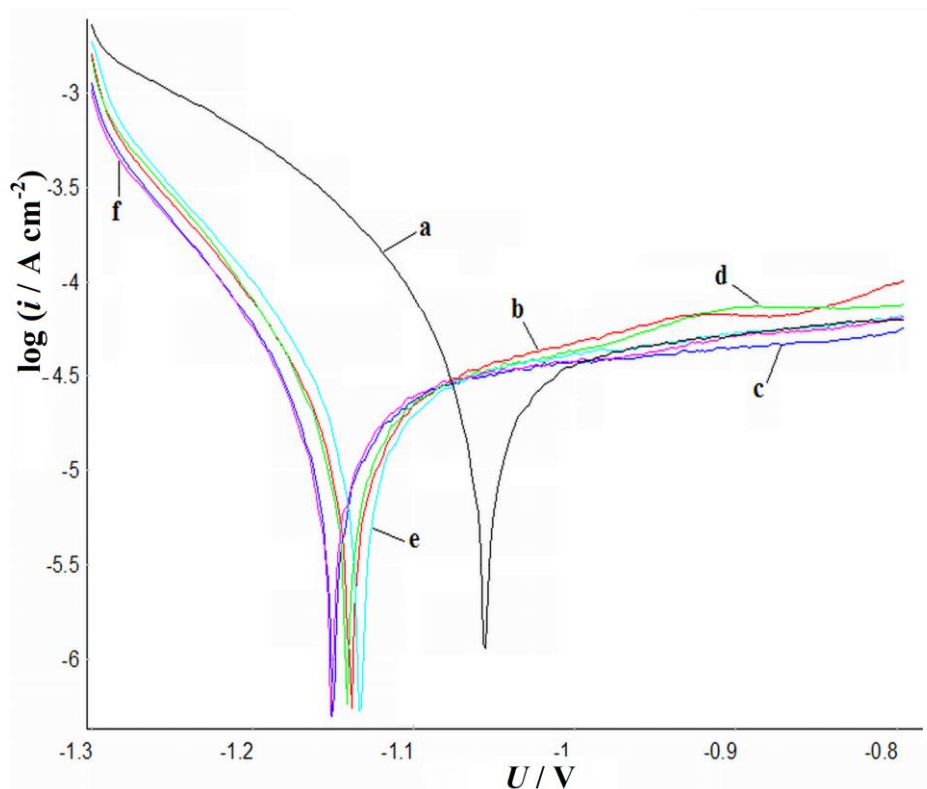
211

212   Fig. 6. Tafel representation of polarization curves recorded in 0.1 M Na_2SO_4 for the studied

213   electrodes. (a) OL, (b) $ZnTa_2O_6$, (c) $ZnNb_2O_6$, (d) $Zn(Ta_{0.95}Nb_{0.05})_2O_6$, (e) $Zn(Ta_{0.9}Nb_{0.1})_2O_6$ and

214   (f) $Zn(Ta_{0.5}Nb_{0.5})_2O_6$

215

216   The slopes were determined in the Tafel region of the anodic and cathodic curves for

217   segments of approximately 50 mV, before and after the corrosion potential (U).

218   The current density corresponds to the rate of electrochemical reactions associated with

219   corrosion processes taking place on OL surface, under polarization in 0.1 M Na_2SO_4 media.

220   Table 2. Tafel parameters of investigated electrodes after 30 minutes immersion in 0.1 M

221   Na_2SO_4 solution.

Electrod	E_{corr} / V	i_{corr} / $\mu A/cm^2$	Rp / kohm x cm²	v_{cor}/ $\mu m/Y$	IE / %
Bare OL	-1.05	40.36	0.90	469.1	-
$ZnTa_2O_6$	-1.14	20.74	1.40	241.1	48.61
$ZnNb_2O_6$	-1.15	19.09	1.41	221.9	52.70
$Zn(Ta_{0.95}Nb_{0.05})_2O_6$	-1.14	23.25	1.34	270.2	42.39

11

| Zn(Ta$_{0.9}$Nb$_{0.1}$)$_2$O$_6$ | -1.13 | 22.51 | 1.27 | 261.7 | 44.22 |
| Zn(Ta$_{0.5}$Nb$_{0.5}$)$_2$O$_6$ | -1.15 | 21.23 | 1.43 | 246.8 | 47.40 |

The corrosion potential (E_{corr}) of the bare OL electrode is -1.05 V and the corresponding corrosion current density (i_{corr}) is 40.36 μA/cm². In all cases the presence of Zn(Ta$_{1-x}$Nb$_x$)$_2$O$_6$ shifted the polarization curves towards the region of lower corrosion current densities because of the better stability of the covering metal oxides. For all studied covering materials a similar corrosion inhibiting activity is observed, as presented in Table 2. The differences in the inhibition efficiencies (*IE*) are probably generated by the differences in the stability of these materials, the roughness and the porosity of the protective coatings. Comparing, for instance, ZnNb$_2$O$_6$ and ZnTa$_2$O$_6$, the average roughness is rising from $S_a = 0.21$nm to $S_a = 0.73$nm and the *IE* decrease from 52.7 % to 48.61 % respectively. Furthermore, ZnNb$_2$O$_6$ has a uniform covering aspect being less porous than ZnTa$_2$O$_6$. This study clearly showed that the decrease of the niobium content in the pseudo-binary oxides accompanied by the increasing of average roughness values has the effect of decreasing the inhibition efficiency.

The shift of E_{corr} toward negative values in the presence of Zn(Ta$_{1-x}$Nb$_x$)$_2$O$_6$ is caused by the different nature of the electrochemically active species from the metal surface (Zn, Ta, Nb) beside Fe. The presence of solely niobium ions next to the zinc ones (the case of ZnNb$_2$O$_6$) shifted the corrosion potential towards more negative values (-1.15 V), the corrosion current density being decreased from 40.36 (OL) to 19.09 μA/cm² that means a decrease of the corrosion rate (v_{cor}) and a better inhibition efficiency.

The polarization resistance (*Rp*) increases slightly from 0.9 kohm x cm² for bare OL to 1.43 kohm x cm² for the Zn(Ta$_{0.5}$Nb$_{0.5}$)$_2$O$_6$ covered electrode, also indicating an inhibition of the corrosion in the presence of Zn(Ta$_{1-x}$Nb$_x$)$_2$O$_6$ nanomaterials.

CONCLUSIONS

Three novel pseudo-binary oxides, namely: Zn(Ta$_{0.5}$Nb$_{0.5}$)$_2$O$_6$, Zn(Ta$_{0.9}$Nb$_{0.1}$)$_2$O$_6$ and Zn(Ta$_{0.95}$ Nb$_{0.05}$)2O$_6$ were obtained by solid-state method and comparatively characterized by XRD, FT-IR, SEM/EDAX, AFM and UV-VIS investigations with already known ZnNb$_2$O$_6$ and ZnTa$_2$O$_6$ compounds.

The existence of a single crystalline phase and the average crystallite size were evidenced from the XRD diagrams and confirmed by the AFM measurements. A strong correlation between the aspect of the samples (SEM images) and the rugosity properties was found. The nanomaterial capacity to agglomerate might justify the continuously and uniform covering of the OL materials.

The structure of the studied materials was confirmed by FT-IR spectra and EDAX analysis. The values of the band gap increased in the order: $ZnNb_2O_6$, $Zn(Ta_{0.5}Nb_{0.5})_2O_6$, $Zn(Ta_{0.9}Nb_{0.1})_2O_6$, $Zn(Ta_{0.95}Nb_{0.05})_2O_6$ and $ZnTa_2O_6$ according to the chemical stability of the tested material and with the increase in tantalum content, recommending these materials for application in photovoltaic cells.

The electrochemical parameters of the Tafel plots illustrate corrosion inhibition in the presence of the all new synthesized $Zn(Ta_{1-x}Nb_x)_2O_6$ compounds deposited on OL surface. Zn oxide combinations with Ta and Nb oxides evidently show that the inhibition efficiency increase with the niobium content of the material. The best results reveal that $ZnNb_2O_6$ treated electrode exhibits an inhibition efficiency of 52.7 %.

Due to the inhibition efficiency of pseudo-binary oxides deposited on carbon steel electrode the nanomaterials with increased niobium content will be used in multiple layer deposition with porphyrins in order to improve anticorrosion properties. Due to the high band gap (3.80-4.30 eV) provided by increasing the tantalum content, four of these pseudo-binary oxides might find applications in photovoltaic cells.

REFERENCES

1. B.H. Ali, B.S. Ali, R.Yusoff, M. K. Aroua, *J. Electrochem. Sci*. **6** (2011) 181

282   2. M. Zemanova, *Chem. Papers* **63** (5) (2009) 574

283   3. S. Yogesha, A. C. Hegde, *Transactions of The Indian Institute of Metals*, **63** (6) (2010)
284   841

285   4. R.N. Jagtap, P.P. Patil, S.Z. Hassan, *Prog. Org. Coat.* **63** (2008) 389

286   5. A.P. Patil, R.H. Tupkary, *Transactions of The Indian Institute of Metals* **62** (1) (2009) 71

287   6. A.Roshanghias, M. Heydarzadeh Sohi, *J. Coat. Technology. Res.* **9** (2) (2012) 215

288   7. H. Shi, F. Liu, E. Han, Y. Wei, *J. Mater. Sci. Technol.* **23** (4) (2007) 551

289   8. Q. An, Y. Xinb, K. Huo, X. Cai, P. K. Chu, *Mater. Chem. Phys.* **115** (2009) 439

290   9. A.P. I. Popoola, O. S. I. Fayomi, *International J. Phys. Sci.* **6** (10) (2011) 2447

291   10. A.E. Elsherief, M.A. Shoebi, *J. Corrosion Prev. Control* (2003) 25

292   11. R.A. Grahan, R.C. Sutherlin, *Proceedings of the international Symposium Niobium 2001*,
293   Ltd, Bridgeville, USA, (2001) 337

294   12. J.-P. Masse, H. Szymanowski 1, O. Zabeida, A. Amassian, J.E. Klemberg-Sapieha, L.
295   Martinu, *Thin Solid Films* **515** (2006) 1674

296   13. K. Kamada, M. Mukai, Y. Matsumoto, *Electrochim. Acta* **49** (2004) 321

297   14. J.H. Plrk, S. Nahm, J.G. Park, *J. Alloys Compd.*, **537** (2012) 221

298   15. Y.C. Zhang, B.Fu, X. Wang, *J. Alloys Compd.*, **478** (2009) 498

299   16. S. Wu, J. Luo, *J. Alloys Compd.*, **509** (2011) 8126

300   17. W.-S. Xia, G.-Y. Zhang, L.-W. Shi, M.-M. Zhang, *Mater. Lett.* **124** (2014) 64

301   18. B. Fu,Y. Zhang, H.Yue, *Ceram. Int.* **39** (2013) 3789

302   19. Y. C. Zhang, B. J. Fu, X. Wang, *J. Alloys Compd.*, **478** (2009) 498

303   20. Y. NuLi, Z.-W. Fu, Y.-Q. Chu, Q.-Z. Qin, *Solid State Ionics* **160** (2003) 197

304   21. M. Bîrdeanu, A.-V. Bîrdeanu, E. Fagadar-Cosma, C. Enache, I. Miron, I. Grozescu,, *Dig*
305   *J Nanomater Bios*, **8** (2013) 263

306   22. Y.C. Zhang, Z.X. Yue, X. Qi, B. Li, Z.L. Gui, L.T. Li, *Mater. Lett.* **58** (2004) 1392.

307   23. H. B. Bafrooei, E. T. Nassaj, T. Ebadzadeh, C. Hu, *Ceram. Int.* **40** (2014) 14463

308   24. G. Feng, L. Jiaji, H. Rongzi, L. Zhen, T. Changsheng, *Ceram. Int.* **35** (2009) 2687

309   25. L. Guo, J. Dai, J. Tian, Z. Zhu, T. He, *Mater. Res. Bull.* **42** (2007) 2013

310   26. L. Guo, J. Dai, J. Tian, T. He, *Ceram. Int.* **34** (2008) 1783

311   27. C.-H. Hsu, P.-C. Yang, H.-W. Yang, S.-F. Yan, H.-H. Tung, *Thin Solid Films* **519** (2011)
312   5030

313   28. L.B. Kong, J. Ma, H. Huang, R.F. Zhang, T.S. Zhang, *J. Alloys Compd*. **347** (2002) 308.

314   29. D. Xu, Y. Liu, Q. Zhou, T. Cui, H. Yuan, W. Wang, Z Shi, L. Li, *J. Alloys Compd*. **618**

315   (2015) 694

316   30. W. Wu, S. Liang, Z. Ding, H. Zheng, L. Wu, *Solid State Sciences* **13** (2011) 2019

317   31. L. Zhang, I. Djerdj, M. Cao, M. Antonietti, M. Niederberger, *Adv. Mater.* **19** (2007) 2083

318   32. Z. Ding, W. Wu, S. Liang, H. Zheng, L. Wu, *Mater. Lett*. **65** (2011) 1598

319   33. S. Liang, L. Wu, J. Bi, W. Wang, J. Gao, Z. Li, X. Fu, *Chem. Commun*. **46** (2010) 1446

320   34. D. Chen, J. Ye, *Chem. Mater.* **21** (2009) 2327

321   35. K. Saito, A. Kudo, *Inorg. Chem.* **49** (2010) 2017

322   36. S. A. Anggraini, M. Breedonb, N. Miura, *Sens. Actuators, B* **187** (2013) 58

323   37. T. Wang, X. Wei, Q. Hu, L. Jin, Z. Xu, Y. Feng, *Mater. Sci. Eng., B* **178** (2013) 1081

324   38. Y.-J. Hsiao, T.-H. Fang, L.-W. Ji, *Mater. Lett.* **64** (2010) 2563

325   39. M. Birdeanu, A. – V. Birdeanu, I. Popa, B. Taranu, F. Peter, I. Creanga, A. Palade, E.

326   Fagadar-Cosma, *NANOCON 2014, Conference Proceedings*, (2015) TANGER Ltd.,

327   Ostrava, Czech Republic, 262-268, ISBN 978-80-87294-53-6

328   40. Z. Ahmad, *Principles of Corrosion Engineering and Corrosion Control*, Butterworth-

329   Heinemann/IChemE Series. Elsevier, Amsterdam, (2006) p. 377-396

330   41. S. K. Kurinec, P. D. Rack, M. D. Potter, T. N. Blanton, *J. Mater. Res*., **15** (6) (2000) 1320

331   42. www.ill.eu/sites/fullprof/

332   43. T. Minami, H. Sato, K. Ohashi, T. Tomofuji, and S. Takata, *J. Cryst.Growth* **117** (1992)

333   370

334   44. M. Bîrdeanu, A.-V. Bîrdeanu, A.S. Gruia, E. Fagadar-Cosma, C.N. Avram, *J Alloy.*

335   *Comp*. **573** (2013) 53

336   45. V. Kapaklis, P. Poulopoulos, V. Karoutsos, Th. Manouras, C. Politis, *Thin Solid Films*,

337   **510** (2006) 138

338   46. P. Kubelka, F. Munk, *Zh. Tekh. Fiz*. **12** (1931) 593

339   47. P. Kubelka, *J. Opt. Soc. Am.* **38** (1948) 448